ROYAL SOCIETY
OF CHEMISTRY

PAPER

Check for updates

Acid-triggered *in vivo* aggregation of Janus nanoparticles for enhanced imaging-guided photothermal therapy†

Ruixue Wei, ID *a Zhe Li,a Bilun Kang,b Gaoliang Fu,c Ke Zhang ID *d and Mengzhou Xue ID *a

Poor tumor delivery efficiency remains a significant challenge for the integrated nanoplatform for diagnosis and treatment. Nanotherapeutics capable of aggregation in response to the tumor microenvironment has received considerable attention because of its ability to enhance tumor delivery efficiency and accumulation. We prepared smart Au–Fe$_3$O$_4$ Janus nanoparticles (GIJ NPs) modified with mixed-charged ligands (3,4-dihydroxyhydrocinnamic acid [DHCA] and trimethylammonium dopamine [TMAD]). The obtained GIJ@DHCA-TMAD could be stable at the pH of the blood and normal tissues, but aggregated into larger particles in response to the tumor acidic microenvironment, leading to greatly enhanced accumulation in cancer cells. The hydrodynamic diameters of GIJ@DHCA-TMAD increased from 28.2 to 105.7 nm when the pH decreased from 7.4 to 5.5. Meanwhile, the T_2 magnetic resonance imaging (MRI) contrast capability, photoacoustic imaging (PAI) performance, and photothermal conversion efficiency of GIJ@DHCA-TMAD were also enhanced with increasing diameter. Tumor-specific enhanced MRI and PAI can precisely locate tumor boundaries and can be used to perform preliminary photothermal tumor ablation therapy: the pH-sensitive GIJ@DHCA-TMAD can be used in dual-mode, tumor-specific imaging-guided photothermal therapy to better meet the multiple requirements for *in vivo* applications.

Introduction

Over the past decade, the integration of diagnostic and therapeutic functions into a single nanoplatform through nanotechnology has attracted much attention because of its potential to personalize therapy in an efficient manner.[1–4] Although significant progress has been made in various types of nanotherapeutic platforms,[5–8] enormous challenges remain for applications in complex biological systems. For example, traditional nanomedicines produce poor targeting in tumor tissues, resulting in poor delivery efficiency and thus affecting efficacy. Larger nanoparticles (NPs > 100 nm) can passively target tumor tissue by the enhanced permeability and retention (EPR) effect, resulting in improved tumor targeting and accumulation.[9] However, because of the dense extracellular matrix and elevated interstitial fluid pressure in tumor tissue,[10] large NPs cannot fully penetrate deep into the tumor tissue, resulting in suboptimal delivery. Additionally, increasing the size of NPs also triggers the recognition and rapid clearance of NPs by the mononuclear macrophage system (MPS), which greatly impairs the blood circulation time of NPs.[11] Small NPs (<20 nm) have good tumor penetration and can diffuse more uniformly within tumor tissue. However, even small NPs that penetrate deep into tumor tissue still have a high chance of backflow and rapid excretion from the body, resulting in insufficient accumulation in tumors.[11]

To better meet the needs of biomedical applications, improving the tumor targeting of nanomedicines remains a major challenge. Ideal nanomedicines tend to possess the following properties:[12] (1) good biocompatibility,[13,14] (2) excellent stability and long blood circulation time,[15] (3) high tumor targeting and accumulation,[16] and (4) fast clearance rates in normal tissues.[17] These features ensure high tumor specificity

aDepartment of Cerebrovascular Diseases, The Second Affiliated Hospital of Zhengzhou University, Zhengzhou 450052, Henan, China. E-mail: wei2009ruixue@163.com; xuemengzhou@zzu.edu.cn

bState Key Laboratory of Physical Chemistry of Solid Surfaces, The MOE Laboratory of Spectrochemical Analysis & Instrumentation, The Key Laboratory for Chemical Biology of Fujian Province, College of Chemistry and Chemical Engineering, Xiamen University, Xiamen 361005, Fujian, China

cHenan Provincial Key Laboratory of Nanocomposites and Applications, Institute of Nanostructured Functional Materials, Huanghe Science and Technology College, Zhengzhou 450006, Henan, China

dDepartment of Interventional Medicine, Center for Interventional Medicine, Guangdong Provincial Engineering Research Center of Molecular Imaging, Guangdong Provincial Key Laboratory of Biomedical Imaging, The Fifth Affiliated Hospital, Sun Yat-sen University, Zhuhai 519000, Guangdong, China. E-mail: zhangk276@mail.sysu.edu.cn

† Electronic supplementary information (ESI) available: Materials and methods, XPS, DLS, biodistribution, and H&E staining. See DOI: https://doi.org/10.1039/d2na00622g
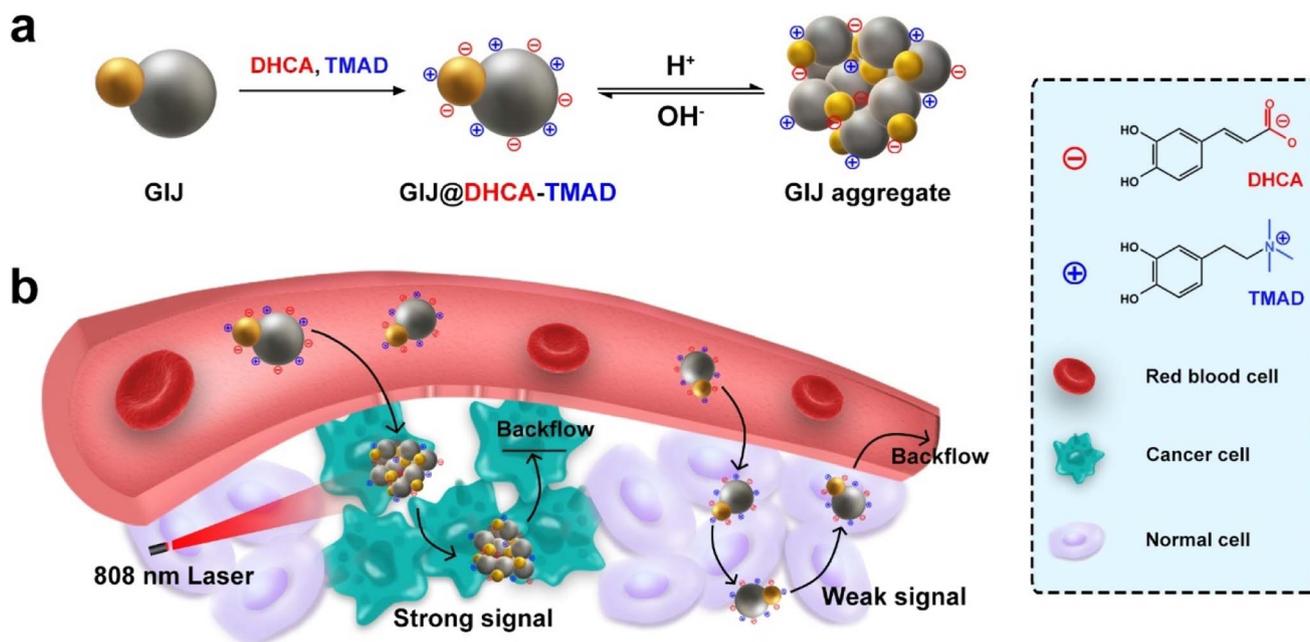
Scheme 1 Schematic illustration of (a) acid-induced aggregation and (b) *in vivo* behavior of GIJ@DHCA-TMAD after intravenous injection for enhanced tumor accumulation and MR/PA imaging-guided PTT of tumors.

while minimizing side effects. However, the size and surface charge of existing traditional nanomedicines are almost unchanged, making it difficult for them to meet all expectations noted above simultaneously in complex biological systems. After intravenous administration, traditional nanomedicines cannot change their properties with the environment to achieve optimal tumor targeting, thus, they cannot produce the best therapeutic effect. Therefore, it is urgent to develop new strategies to enable NPs to adaptively change their properties to meet individualized needs and produce optimal therapeutic effects. Recently, the modification of mixed-charged ligands enabled *in situ* aggregation of NPs under specific pH conditions by tuning the ratio between positive and negative charges.[12,18–20] This may provide an opportunity to achieve the above-mentioned goals. The unique weak acidity[5,21] of the tumor microenvironment (TME) can be used to manipulate the *in situ* aggregation of small NPs. The NPs maintain a small size in blood circulation and preserve the clearance advantages, but aggregate in the TME. After delivery to the tumor, the aggregated NPs are restricted from flowing back into the vasculature.

Iron oxide NPs have received extensive attention as magnetic resonance imaging (MRI) contrast agents because of their good biocompatibility, magnetic properties, and aggregation of iron oxide NPs that significantly enhance their T_2 performance.[22–26] Gold NPs have the characteristics of excellent biocompatibility, strong light absorption, good photothermal conversion ability, and easy synthesis. Particularly, the light absorption of Au NPs can be shifted to the red or near-infrared (NIR) region by modulating their size, which makes Au NPs ideal not only for photothermal therapy (PTT) but also for use in photoacoustic imaging (PAI) promising candidates. Aggregation of Au NPs promotes the formation of interparticle "hot spots" and significantly increases the localized surface plasmon resonance coupling of Au NPs,[27,28] enhancing the self-PAI signal and PTT efficacy.[29,30]

In this study, we describe the development of gold–iron oxide Janus (GIJ) NPs by a one-pot method. GIJ NPs was further functionalized with two oppositely charged ligands, 3,4-dihydroxyhydrocinnamic acid (DHCA) and trimethylammonium dopamine (TMAD), resulting in a mixed-charged surface (Scheme 1a). As described in Scheme 1b, in blood and normal tissues, small GIJ@DHCA-TMAD maintains good dispersion and circulates stably *in vivo*. Once localized at the tumor, GIJ@DHCA-TMAD can penetrate into tumor tissue and aggregate, significantly enhancing passive tumor targeting by the EPR effect, and be trapped in the tumor. Additionally, *in situ* aggregation of GIJ@DHCA-TMAD in the tumor will also enhance the MRI and PAI signal differences between the tumor and surrounding normal tissue, improving the accuracy of tumor boundary identification. Moreover, the aggregated GIJ@DHCA-TMAD triggered effective PTT in the tumor, with minimal adverse effects on normal tissue after NIR laser irradiation.

Results and discussion

Synthesis and characterization

We prepared GIJ NPs by one-pot thermal decomposition of iron acetylacetonate and gold acetate in 1-octadecene in the presence of oleylamine, oleic acid, and 1,2-hexadecanediol. The transmission electron microscopy (TEM) image revealed the morphology and size of GIJ NPs (Fig. 1a). The hydrophobic GIJ NPs were Janus structures with a diameter of 19.7 ± 2.8 nm. The elemental mapping of GIJ NPs clearly displayed the distribution of Au and Fe in the Janus structure (Fig. 1b). Inductively coupled plasma atomic emission spectroscopy (ICP-AES) was used to
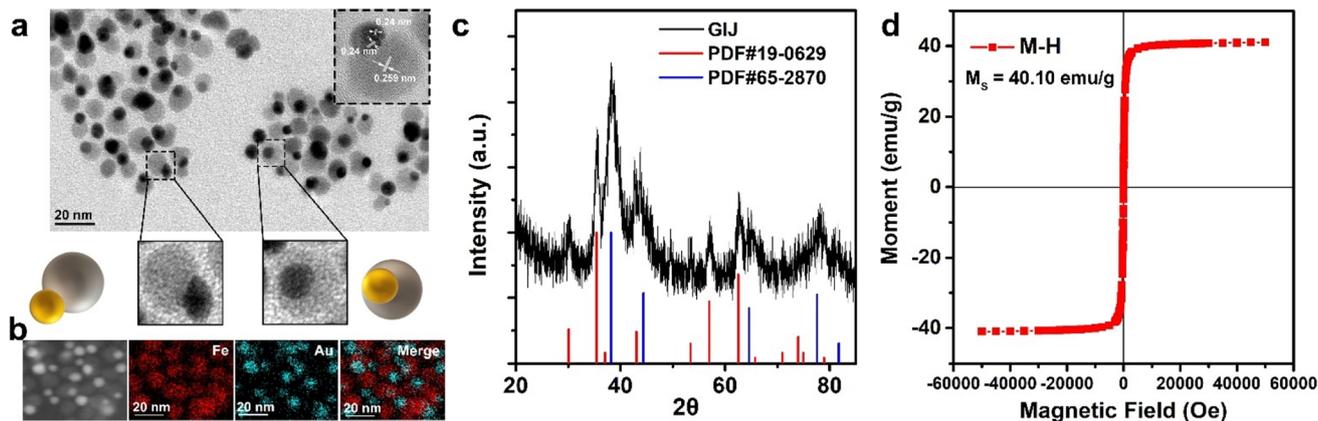
Fig. 1 Characterization of GIJ NPs. (a) The transmission electron microscopy (TEM) images and high-resolution TEM (HRTEM) image (inset) of GIJ NPs. (b) EDX-mapping images and (c) X-ray powder diffraction (XRD) pattern of GIJ NPs, and the standard XRD patterns of Au (JCPDS NO. 19-0629) and Fe_3O_4 (JCPDS NO. 65-2870). (d) Field-dependent magnetization curves (M–H) of GIJ NPs at a magnetic field of 5 T at 300 K.

detect the ratio of elements Au and Fe. The results showed that the molar ratio of Au and Fe is 1.1 : 3.0. X-ray powder diffraction (XRD) revealed the typical crystal structure of gold (JCPDS NO. 19-0629) and magnetite (JCPDS NO. 65-2870; Fig. 1c). X-ray photoelectron spectroscopy (XPS) indicated the surface characteristics of GIJ NPs (Fig. S1†). The peaks of Fe $2p_{3/2}$ (710.8 eV), Fe $2p_{1/2}$ (724.1 eV), Au $4f_{7/2}$ (84.0 eV), and Au $4f_{5/2}$ (87.7 eV) indicated the state of Fe and Au, respectively, which were consistent with XRD results. Next, we assessed the magnetic properties of GIJ NPs using a superconducting quantum interference device (SQUID) at a magnetic field of 5 T at 300 K. Field-

dependent magnetization curves suggested that the obtained NPs possess typical superparamagnetic properties and had a saturation magnetization (M_S) value of 40.10 emu g^{-1} (Fig. 1d), which affects the T_2 relaxation properties of GIJ NPs.

In vitro aggregation ability of GIJ@DHCA-TMAD

To prepare pH-responsive aggregated GIJ NPs, strongly electrolytic positive TMAD (Fig. S2† shows the synthesis step) and weakly electrolytic negative DHCA were used to modify the surface of GIJ NPs. We functionalized GIJ NPs using mixed
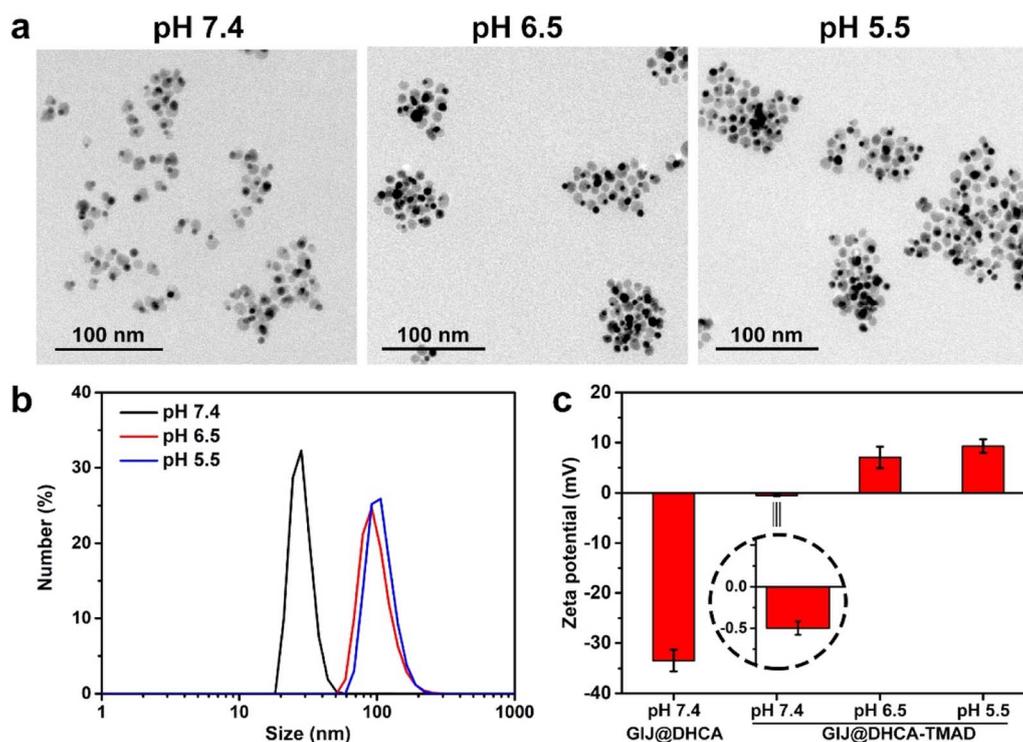

Fig. 2 In vitro acid-induced aggregation of GIJ@DHCA-TMAD. (a) The TEM images and (b) dynamic light scattering (DLS) of GIJ@DHCA-TMAD in 1× PBS buffer at different pH values (7.4, 6.5, and 5.5). (c) Zeta potential of GIJ@DHCA-TMAD and GIJ@DHCA.

ligands with a molar ratio of DHCA to TMAD of 4.5 : 1 *via* the ligand exchange method. As shown in Fig. 2a, TEM images of GIJ@DHCA-TMAD at different pH values showed that GIJ@DHCA-TMAD has sizes ranging from 60 to 120 nm (pH 6.5) and 80 to 200 nm (pH 5.5). The hydrodynamic diameters (HDs) also corroborated the results of TEM (Fig. 2b). For comparison, the non-sensitive ligand, DHCA was covalently bound on the surface of GIJ NPs, and the HDs of GIJ@DHCA remained almost unchanged at different pH values (Fig. S3†).

Considering the effect of NP surface charge *in vivo* behavior,[31] we also measured the surface charges of GIJ@DHCA-TMAD at 7.4, 6.5, and 5.5 (Fig. 2c). The zeta potential of GIJ@DHCA-TMAD and GIJ@DHCA was −0.49 and −33.45 mV at pH 7.4, respectively. The zeta potential of GIJ@DHCA-TMAD shifted from −0.49 to 6.18 to 7.80 mV when the pH changed from 7.4 to 6.5 to 5.5, respectively. The coexisting carboxyl and amine groups on an NP lead to a zwitterionic-like system that is pH-responsive.[12,32] It is possible to destabilize dispersed GIJ@DHCA-TMAD and promote aggregation of NPs by adjusting to certain pH conditions, which may be the result of the competition of van der Waals attraction, hydrogen bond attraction, electrostatic repulsion, hydration repulsion, and other forces (Fig. S4†).[33] In this study, the changes in GIJ@DHCA-TMAD surface charge at diverse pH values indicated that pH changes induced protonation and deprotonation of functional groups, and the interaction forces between nanoparticles changed, which eventually led to the aggregation of GIJ@DHCA-TMAD. Additionally, negatively charged or neutral NPs exhibit prolonged blood circulation and enhanced tumor accumulation but cannot be effectively internalized by tumor cells.[31,34] By contrast, positively charged NPs facilitate cellular uptake, but they are readily eliminated from blood circulation by the MPS.[31,34] In this study, GIJ@DHCA-TMAD underwent a change from neutral to positive charge at pH 5.5, rendering it inert or stealthy in blood circulation but activated to be recognized by tumor cells after accumulation in the tumor tissue. Of note, the HDs of GIJ@DHCA-TMAD did not change significantly even after 7 days of incubation in phosphate buffer (1× PBS, pH = 7.4) and 10% (v/v) fetal bovine serum (FBS) solution (Fig. S5†), which implied that GIJ@DHCA-TMAD had high stability in a neutral environment and perfect nonspecific adsorption resistance just as single-component zwitterionic NPs.[35,36] We also recorded the UV-vis spectra of GIJ@DHCA-TMAD at pH 7.4 and 5.5 (Fig. S6†), indicating that the absorption in the NIR window increased with decreasing pH because of particle aggregation, which is beneficial for enhancing photothermal conversion efficiency.

In vitro relaxivity measurement

To evaluate the pH-responsive MRI behavior, we subsequently tested the relaxation effectiveness of GIJ@DHCA-TMAD at various pH values on a 0.5 T MR scanner, and used GIJ@DHCA for comparison (Fig. 3a and b and S7†). The results showed r_2 values of 34.6 ± 0.4 and 35.6 ± 0.2 m M^{-1} s^{-1}, respectively, for GIJ@DHCA-TMAD and GIJ@DHCA at pH 7.4. There was no appreciable distinction in r_2 values of GIJ@DHCA-TMAD and GIJ@DHCA at pH 7.4. The r_2 values of GIJ@DHCA-TMAD (281.2 ± 1.8 m M^{-1} s^{-1}), however, were significantly increased at pH 5.5, whereas the r_2 values of GIJ@DHCA (31.7 ± 0.3 m M^{-1} s^{-1}) were almost unchanged. T_2-weighted images also suggested that GIJ@DHCA-TMAD had stronger T_2 signals at pH 5.5 than at pH 7.4 with the same Fe concentration (Fig. 3c). Conversely, the T_2 signals of GIJ@DHCA at pH 5.5 and 7.4 were not significantly different at the same Fe concentration (Fig. 3d). These results indicated that the T_2 performance was enhanced after acid-induced aggregation of GIJ@DHCA-TMAD, which is consistent with previously reported results.[22,32]
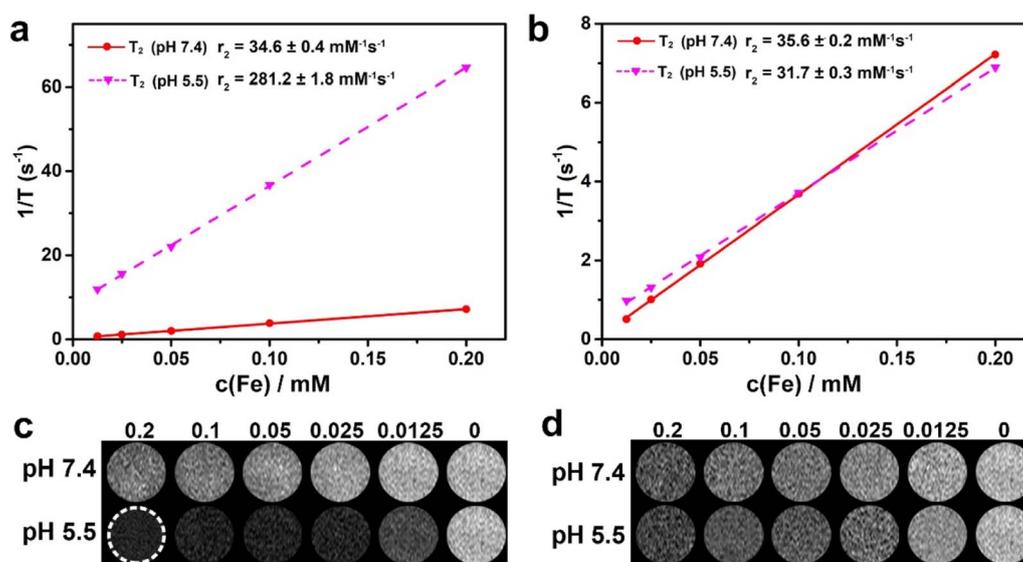

Fig. 3 *In vitro* MRI performance. Relaxation measurements of (a) GIJ@DHCA-TMAD and (b) GIJ@DHCA at 0.5 T. T_2-weighted phantom imaging of (c) GIJ@DHCA-TMAD and (d) GIJ@DHCA on a 0.5 T MRI scanner.

Photothermal conversion performance

Considering that the aggregation of GIJ@DHCA-TMAD at pH 5.5 could lead to a strong absorption band in the NIR region (Fig. S6†),[12,37] this would enhance the photothermal conversional efficiency of GIJ@DHCA-TMAD, which would be beneficial to the improvement of PTT efficacy and the PAI signal. We then measured the photothermal conversion efficiency of GIJ@DHCA-TMAD at different pH values under continuous laser irradiation and recorded the temperature in real time (Fig. 4a and b). After 5 min of 808 nm laser irradiation, the temperature of GIJ@DHCA-TMAD (160 µg Au per mL) increased by 28.4 °C at pH 7.4, whereas the temperature raised by 32.5 °C at a pH of 5.5. The temperature of GIJ@DHCA-TMAD solution at pH 5.5 reached 58 °C, which is beyond the temperature tolerance of tumor cells.[38,39] Additionally, GIJ@DHCA-TMAD exhibited concentration-dependent photothermal conversion behavior at both pH 7.4 and 5.5. At the same concentration, the temperature of GIJ@DHCA-TMAD was proportional to the laser power density (Fig. 4c). In addition, we also calculated the photothermal conversion efficiency of GIJ@DHCA-TMAD to be 77.5% (Fig. S8†). These results show that GIJ@DHCA-TMAD exhibited inferior photothermal properties in blood and normal tissues than in tumor tissues. Once entering the tumor, the photothermal effect can be activated to kill cancer cells at a high temperature.

Live/dead staining was used to detect the photothermal effect of GIJ@DHCA-TMAD on 4T1 cells. Four groups (blank, laser only, GIJ@DHCA-TMAD + laser, and GIJ@DHCA + laser) were used to demonstrate the photothermal effect. After treatment for 4 h and then being exposed to an 808 nm laser at 1 W cm^{-2} for 5 min, the cells were stained with calcein AM (green) and propidium iodide (PI, red) to assess cell viability. The cells treated with GIJ@DHCA-TMAD and laser exhibited stronger red fluorescence than cells in the other groups (Fig. 4d and S9†). Furthermore, after irradiation, a clear boundary between the area of live cells and dead cells was observed, and most of the cells within the laser irradiation site were killed (Fig. 4e and S9†). Additional quantified results were demonstrated using Cell Counting Kit-8 (CCK8), as depicted in Fig. 4f, showing the remarkable cell lethality of GIJ@DHCA-TMAD combination under laser irradiation compared with GIJ@DHCA because of the higher photothermal conversion efficiency generated by GIJ@DHCA-TMAD aggregation. Notably, both GIJ@DHCA-TMAD and GIJ@DHCA had good biocompatibility in the absence of NIR laser irradiation. *In vitro* results suggested that GIJ@DHCA-TMAD with high photothermal conversion capacity could effectively kill cancer cells under NIR laser irradiation.

Biodistribution study

The amount of diagnostic and therapeutic agents accumulated in tumors affects tumor-specific imaging and PTT efficacy *in*
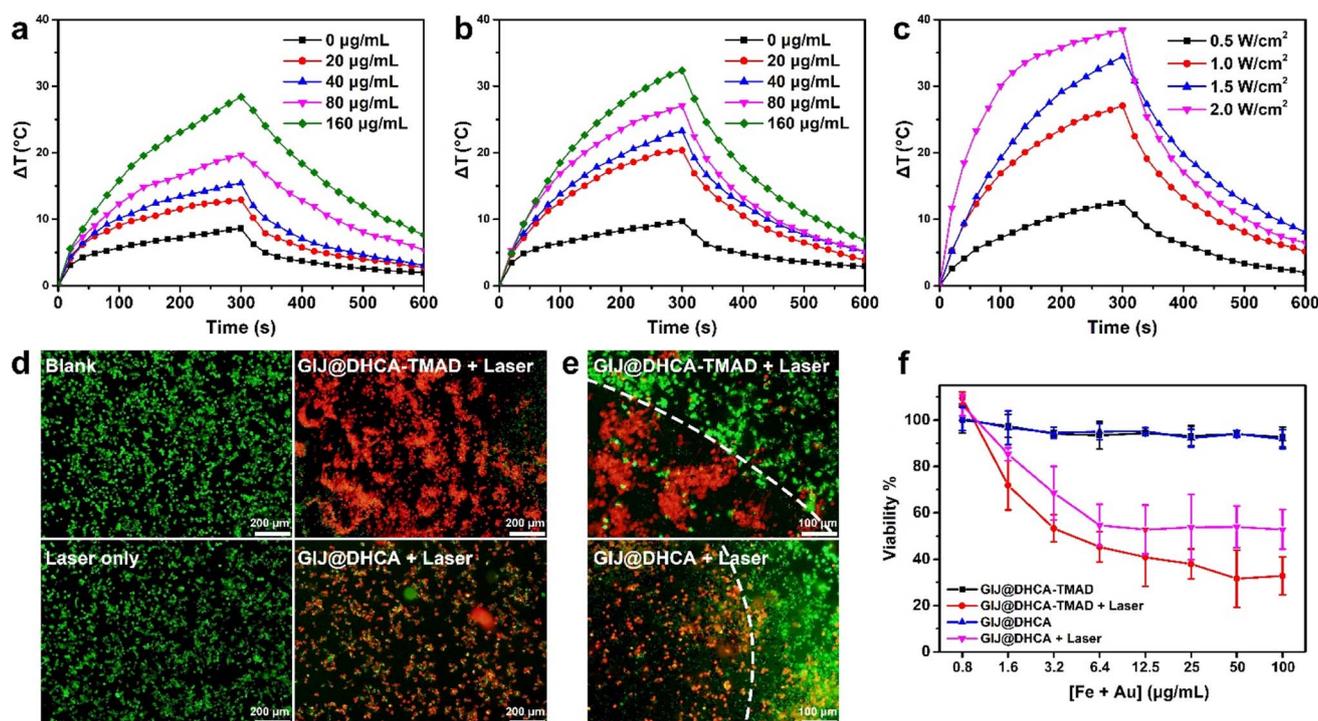

Fig. 4 Photothermal conversion capacity and cytotoxicity. Temperature variation of GIJ@DHCA-TMAD at (a) pH 7.4 and (b) pH 5.5 with different concentrations after 808 nm laser irradiation (1 W cm^{-2}). (c) Temperature variation of GIJ@DHCA-TMAD at pH 5.5 (80 µg mL^{-1}) exposed to 808 nm lasers of different power densities. (d) Fluorescence images of 4T1 cells stained with calcein AM/PI kit for showing the thermal ablation effects of GIJ@DHCA-TMAD and GIJ@DHCA with 808 nm laser irradiation (1 W cm^{-2}, 5 min). The merged fluorescence image of 4T1 cells after treatment with GIJ@DHCA-TMAD or GIJ@DHCA and laser irradiation. (e) The boundary between red (PI, dead cells) and green (calcein AM, live cells) fluorescence corresponded to the laser irradiation spot. (f) The 4T1 cell viability after various treatments.

vivo. To investigate the uptake of GIJ@DHCA-TMAD by tumors, we subsequently evaluated the *in vivo* biodistribution by measuring the Au ion concentration in the major organs using inductively coupled plasma-mass spectrometry (ICP-MS). Before evaluating the biodistribution, we measured the blood circulation of GIJ@DHCA-TMAD using healthy mice. As shown in Fig. S10,† we used a two-compartment model to calculate the blood circulation half-life ($t_{1/2\alpha}$) of the distribution phases of GIJ@DHCA-TMAD and GIJ@DHCA in mice to be 1.2 and 1.1 h, respectively. The $t_{1/2\beta}$ of the elimination phases of GIJ@DHCA-TMAD and GIJ@DHCA in mice was calculated to be 25.1 and 14.4 h, respectively. We noticed that the $t_{1/2\alpha}$ of GIJ@DHCA-TMAD was very close to that of GIJ@DHCA, suggesting that GIJ@DHCA-TMAD did not aggregate into large particles in the blood circulation of healthy mice. However, the $t_{1/2\beta}$ of GIJ@DHCA-TMAD was longer than that of GIJ@DHCA, indicating that GIJ@DHCA-TMAD is widely distributed in the body and likely accumulate in specific tissues.

For biodistribution, GIJ@DHCA-TMAD or GIJ@DHCA was injected into 4T1 tumor-bearing mice. GIJ@DHCA-TMAD achieved a higher level of accumulation in the tumor 24 h after intravenous administration than GIJ@DHCA (3.97 ± 1.50 %ID g^{-1} *vs.* 0.81 ± 0.45 %ID g^{-1}, Fig. S10b†). These pharmacokinetic results indicated that the aggregation of GIJ@DHCA-TMAD at the tumor could enhance the accumulation by the EPR effect and reduce the backflow into the blood circulation.

In vivo MRI and PAI

Encouraged by the contrast capability in response to the weak acid environment *in vitro* and tumor-enhanced accumulation *in vivo*, the *in vivo* MRI capability of GIJ@DHCA-DHAD as a contrast agent was further evaluated. After injection of GIJ@DHCA-TMAD into 4T1 tumor-bearing mice, T_2-weighted MR images at different time points were acquired on a 4.7 T MR scanner (Fig. 5a). The T_2 contrast signal of the tumor reached a maximum at 2 h and continued for 4 h postinjection, which was confirmed *via* quantification analysis (Fig. 5b). By contrast, mice injected with GIJ@DHCA showed a weaker T_2 contrast signal in the tumor site at 2 h and then experienced a decrease at 4 h. This phenomenon may be due to the fact that GIJ@DHCA-TMAD can self-assemble into large particles in the TME. On the one hand, the aggregates have excellent T_2-MRI performance, and on the other hand, large particles are more easily trapped in the tumor site to prevent backflow, thus greatly improving the intratumoral retention rate of GIJ@DHCA-TMAD. These results indicated that GIJ@DHCA-TMAD could efficiently accumulate in the tumor site and specifically enhance tumor signal contrast in MRI.

To achieve accurate diagnosis in clinical settings, multimodal imaging is usually used. Forty micrograms of GIJ@DHCA-TMAD and GIJ@DHCA were respectively administrated intravenously into the tail vein of 4T1 tumor-bearing
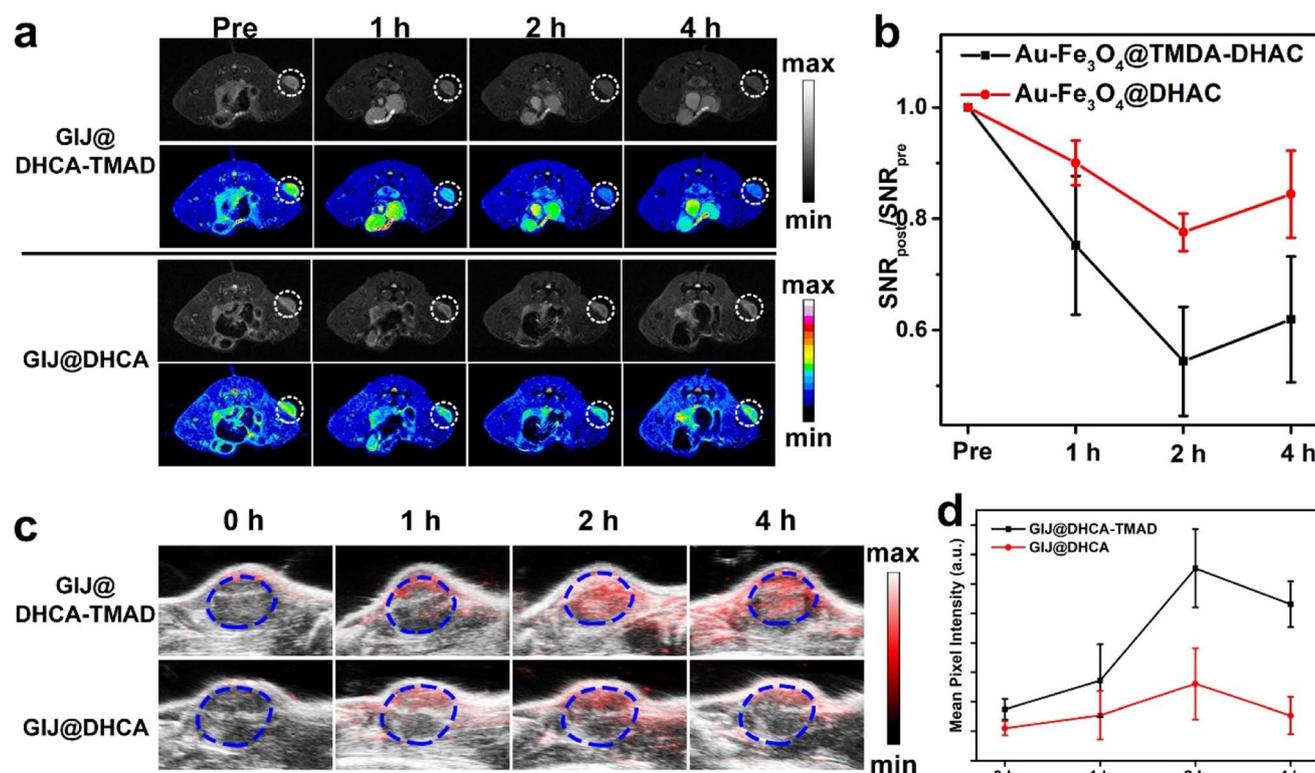

Fig. 5 *In vivo* MR and PA images. (a) *In vivo* T_2-weighted MR images of BALB/c mice before and after intravenous injection of GIJ@DHCA-TMAD or GIJ@DHCA (2 mg Fe per kg body weight) at 4.7 T. The dotted circles indicated the location of the tumor. (b) Quantification of signal-to noise ratio changes (SNR) in the tumor after intravenous injection of GIJ@DHCA-TMAD or GIJ@DHCA at different time points ($n = 3$/group). (c) PA images of the tumor in 4T1 tumor-bearing mice treated with GIJ@DHCA-TMAD or GIJ@DHCA at different time points after intravenous injection. (d) Intensity of the PA signal of tumor regions measured from (c).

mice. As shown in Fig. 5c, in the GIJ@DHCA-TMAD group, a strong signal at the tumor site appeared within 2 and 4 h. By contrast, the PA signal in the tumor site after administration of GIJ@DHCA showed a rapid increase and became invisible within 4 h, which suggested that non-sensitive GIJ@DHCA might be eliminated quickly because of low accumulation in tumor tissue. The PAI results were consistent with MRI results. Moreover, the quantification results in Fig. 5d also revealed the above-mentioned signal regularity, which was consistent with the MRI results. These results demonstrated that GIJ@DHCA-TMAD could aggregate in response to the mild acidic TME, enhance MRI and PAI signals in the tumor, and achieve tumor-specific imaging.

In vivo photothermal therapy study

Encouraged by these results, we next conducted an *in vivo* PTT study on BALB/c nude 4T1 tumor-bearing mice. The mice were randomly divided into 4 groups: the group treated with GIJ@DHCA-TMAD and 808 nm laser irradiation (GIJ@DHCA-TMAD + laser), the group treated with GIJ@DHCA and 808 nm laser irradiation (GIJ@DHCA + laser), the group treated with 808 nm laser only (laser only), and the group treated with PBS. Under the guidance of MRI and PAI, we performed laser irradiation on mice 2 h after intravenous administration, and recorded the temperature changes at the tumor sites during the laser irradiation with a thermal camera (Fig. 6a). As shown in Fig. 6a and b, the temperature increased to 66.7 °C in the GIJ@DHCA-TMAD + laser group, which triggered irreversible tumor damage.[39,40] However, in the GIJ@DHCA + laser and laser only groups, the tumor surface temperatures were 56.1 °C and 44.5 °C, respectively

under the same intensity and time laser irradiation. The superior photothermal effect observed in the GIJ@DHCA-TMAD + laser group could be mainly due to the aggregation and enrichment of GIJ@DHCA-TMAD in the tumor, and the enhanced photothermal conversion performance of aggregated GIJ@DHCA-TMAD.

In vivo anticancer efficacy of GIJ@DHCA-TMAD was then investigated as described in Fig. 6c. Fig. S11† shows the photographs of the mice in the different groups under various treatments. We also monitored the tumor volumes before and after treatment (Fig. 6d). The tumor volume in mice treated with GIJ@DHCA-TMAD and laser irradiation was gradually reduced and almost completely eliminated during treatment. In the GIJ@DHCA + laser group, the solid tumor growth was also inhibited, but the tumor could not be completely ablated. The tumors of mice treated with PBS grew rapidly during treatment. The tumor growth rates in the laser only group decreased relative to the PBS group but did not stop significantly. These results demonstrated that GIJ@DHCA-TMAD and laser irradiation was the most effective treatment modality in this study, because of their efficient accumulation in tumors and enhanced photothermal conversion efficiency. In contrast, the non-sensitive GIJ@DHCA could be pushed back into the blood relatively easily, resulting in poor retention in the tumor. Body weight is a useful indicator for monitoring the health of mice. The average body weight of mice treated with PBS, laser only, or GIJ@DHCA + laser decreased during the treatment period, revealing poor physical condition. However the average body weight of mice treated with GIJ@DHCA-TMAD and laser irradiation remained consistent during the treatment period (Fig. 6e).

The safety assessment of nanomedicines is a key indicator for further biomedical applications. We observed significant tumor
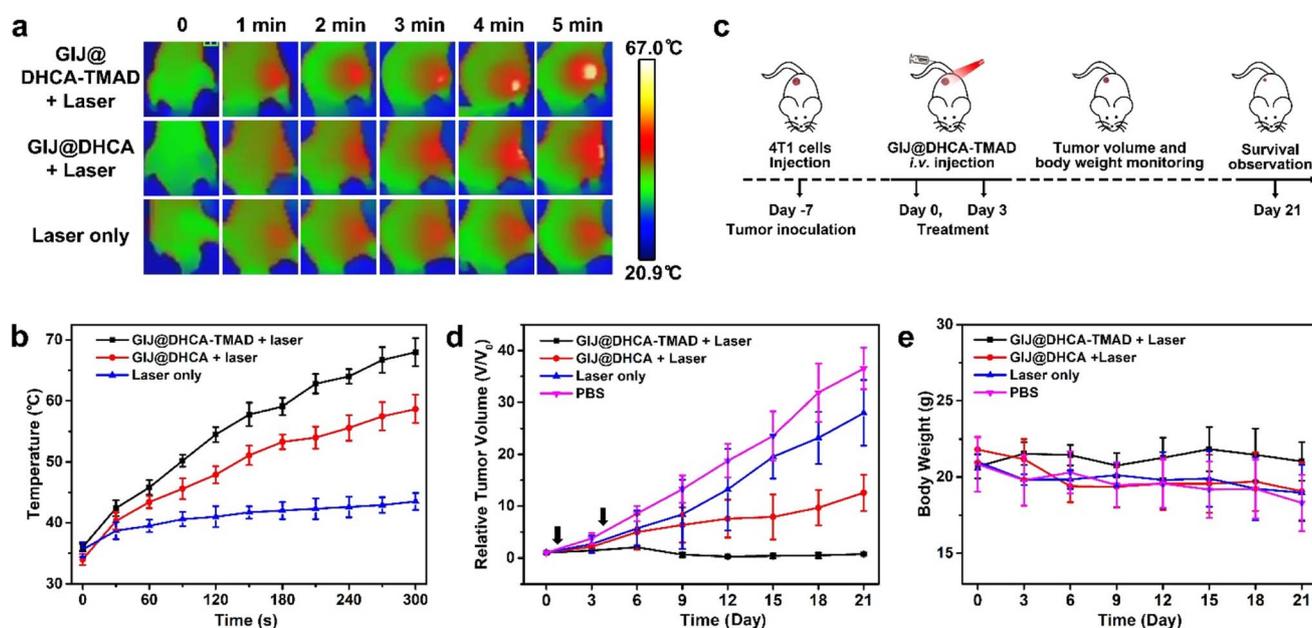

Fig. 6 *In vivo* treatment of mice bearing 4T1 tumors. (a) The infrared thermographic images of mice injected with GIJ@DHCA-TMAD, GIJ@DHCA or PBS under 808 nm laser irradiation (1 W cm^{-2}, 5 min). (b) Temperature changes on the tumor surface recorded by infrared thermography. (c) Schematic illustration of the animal experimental design. (d) Tumor growth curves and (e) average body weight change curves of the mice during various treatments. Arrows indicate the day of treatment ($n = 5$ per group).
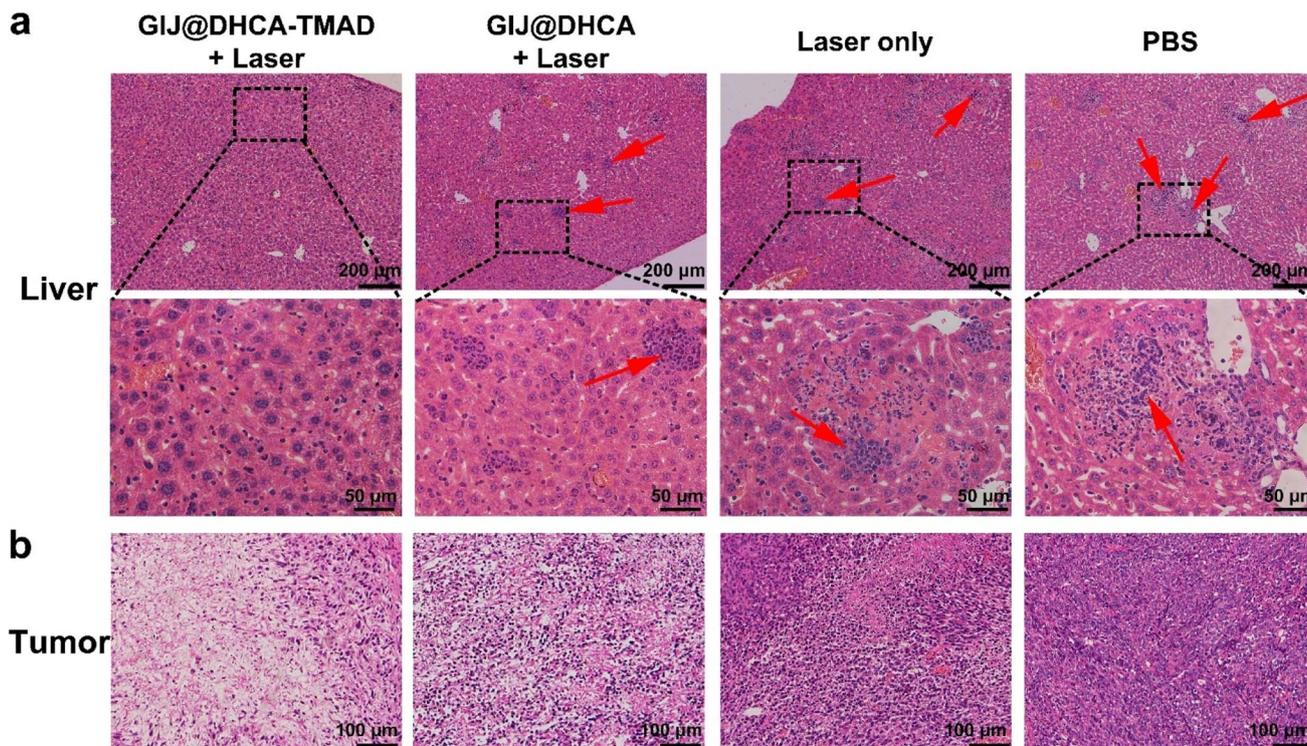
Fig. 7 H&E histology images of the (a) livers and (b) tumors from mice after 30 d treatment. Red arrows indicate the typical liver metastatic tumor cells.

liver metastases in the mice after treatment with laser only and PBS (Fig. S12†), and this distant metastasis indicated an advanced-stage tumor. In the GIJ@DHCA + laser group, the degree of tumor liver metastases was lower than that in the above-mentioned 2 groups, but it was still clearly visible. There was no obvious tumor liver metastasis in the GIJ@DHCA-TMAD + laser group, and the liver surface was smooth and reddish-brown. We then performed hematoxylin and eosin (H&E) staining of major organs and tumors in treated mice to further assess systemic toxicity. Fig. 7a shows H&E staining of the liver, and the red arrows indicate typical liver metastatic tumor cells in the GIJ@DHCA + laser, laser only, and PBS groups. Because of the impaired liver function, the ability of the mice body to synthesize protein decreases, and excess protein and fatty substances in the body are consumed, resulting in weight loss (Fig. 6e). Other organs (heart, spleen, lungs, and kidneys) did not exhibit appreciable microscopic lesions after different treatments (Fig. S13†). The tumor cells were severely damaged in the group of mice treated with GIJ@DHCA-TMAC and laser (Fig. 7b). By contrast, the tumor treated with laser only or PBS showed no damage. These results demonstrated that pH-sensitive GIJ@DHCA-TMAD could kill tumor cells and delay the liver metastasis of tumor cells *in vivo*.

Conclusions

In summary, we developed GIJ NPs by a one-pot thermal decomposition method, and after modification with mixed-charged ligands (DHCA and TMAD), GIJ@DHCA-TMAD exhibited pH-enhanced T_2 MRI and PAI capabilities. GIJ@DHCA-TMAD

could maintain small dispersed NPs in the blood and normal tissue, but would self-assemble into large NPs once it reached the weak acid environment of the tumor. Interestingly, the aggregated GIJ@DHCA-TMAD was capable of improving the accumulation in the tumor and preventing the backflow into the bloodstream. Compared with non-sensitive GIJ@DHCA, the pH-responsive GIJ@DHCA-TMAD had higher tumor accumulation and retention and could effectively inhibit the tumor growth after NIR laser irradiation. Particularly, this enhanced PTT is beneficial for delaying the liver metastasis of tumor cells. The dual-modality, tumor-specific imaging-guided PTT has great potential for accurate diagnosis and precision therapy in biomedical applications.

Author contributions

Conflicts of interest

The authors declare no competing financial interest.

Acknowledgements

References

1 P. H. Cheng and K. Y. Pu, *Nat. Rev. Mater.*, 2021, **6**, 1095–1113.

2 Y. J. Liu, P. Bhattarai, Z. F. Dai and X. Y. Chen, *Chem. Soc. Rev.*, 2019, **48**, 2053–2108.

3 S. M. Dadfar, K. Roemhild, N. I. Drude, S. von Stillfried, R. Knuchel, F. Kiessling and T. Lammers, *Adv. Drug Delivery Rev.*, 2019, **138**, 302–325.

4 K. Liu, Z. Cai, X. Chi, B. Kang, S. Fu, X. Luo, Z.-W. Lin, H. Ai, J. Gao and H. Lin, *Nano Lett.*, 2022, **22**, 3219–3227.

5 R. Wei, X. Gong, H. Lin, K. Zhang, A. Li, K. Liu, H. Shan, X. Chen and J. Gao, *Nano Lett.*, 2019, **19**, 5394–5402.

6 J. L. Wang, L. H. Sui, J. Huang, L. Miao, Y. B. Nie, K. S. Wang, Z. C. Yang, Q. Huang, X. Gong, Y. Y. Nan and K. L. Ai, *Bioact. Mater.*, 2021, **6**, 4209–4242.

7 M. Y. Zhang, X. J. Liu, Q. Luo, Q. Wang, L. J. Zhao, G. Y. Deng, R. B. Ge, L. Zhang, J. Q. Hu and J. Lu, *Chem. Eng. J.*, 2020, **389**, 124450.

8 S. Z. Zhao, X. J. Yu, Y. N. Qian, W. Chen and J. L. Shen, *Theranostics*, 2020, **10**, 6278–6309.

9 V. P. Chauhan and R. K. Jain, *Nat. Mater.*, 2013, **12**, 958–962.

10 M. Sarntinoranont, F. Rooney and M. Ferrari, *Ann. Biomed. Eng.*, 2003, **31**, 327–335.

11 J. Wang, W. Mao, L. L. Lock, J. Tang, M. Sui, W. Sun, H. Cui, D. Xu and Y. Shen, *ACS Nano*, 2015, **9**, 7195–7206.

12 R. Zhang, L. Wang, X. Wang, Q. Jia, Z. Chen, Z. Yang, R. Ji, J. Tian and Z. Wang, *Adv. Healthcare Mater.*, 2020, **9**, 2000394.

13 R. De, M. K. Mahata and K. T. Kim, *Adv. Biosci.*, 2022, **9**, 2105373.

14 R. Zhao, J. Xiang, B. Wang, L. Chen and S. W. Tan, *Bioinorg. Chem. Appl.*, 2022, **2022**, 2444516.

15 T. Ma, R. Chen, N. N. Lv, Y. Chen, H. M. Qin, H. Jiang and J. T. Zhu, *Small*, 2022, **18**, 2106291.

16 H. Ao, Z. Wang, L. K. Lu, H. W. Ma, H. W. Li, J. X. Fu, M. Z. Li, M. H. Han, Y. F. Guo and X. T. Wang, *J. Nanobiotechnol.*, 2022, **20**, 137.

17 L. J. C. Albuquerque, V. Sincari, A. Jager, J. Kucka, J. Humajova, J. Pankrac, P. Paral, T. Heizer, O. Janouskova, I. Davidovich, Y. Talmon, P. Pouckova, P. Stepanek, L. Sefc, M. Hruby, F. C. Giacomelli and E. Jager, *J. Controlled Release*, 2021, **332**, 529–538.

18 X. Liu, Y. Chen, H. Li, N. Huang, Q. Jin, K. Ren and J. Ji, *ACS Nano*, 2013, **7**, 6244–6257.

19 X. Liu, H. Huang, Q. Jin and J. Ji, *Langmuir*, 2011, **27**, 5242–5251.

20 D. F. Hu, H. Li, B. L. Wang, Z. Ye, W. X. Lei, F. Jia, Q. Jin, K. F. Ren and J. Ji, *ACS Nano*, 2017, **11**, 9330–9339.

21 R. A. Gatenby and R. J. Gillies, *Nat. Rev. Cancer*, 2004, **4**, 891–899.

22 Z. Zhou, R. Tian, Z. Wang, Z. Yang, Y. Liu, G. Liu, R. Wang, J. Gao, J. Song, L. Nie and X. Chen, *Nat. Commun.*, 2017, **8**, 15468.

23 S. Fu, Z. Cai and H. Ai, *Adv. Healthcare Mater.*, 2020, **10**, 2001091.

24 R. Wei, T. Zhou, C. Sun, H. Lin, L. Yang, B. W. Ren, Z. Chen and J. Gao, *Nanoscale*, 2018, **10**, 18398–18406.

25 J. Gao, H. Gu and B. Xu, *Acc. Chem. Res.*, 2009, **42**, 1097–1107.

26 J. Lu, J. Sun, F. Li, J. Wang, J. Liu, D. Kim, C. Fan, T. Hyeon and D. Ling, *J. Am. Chem. Soc.*, 2018, **140**, 10071–10074.

27 X. Y. Fang, K. H. Lui, S. Y. Li, W. S. Lo, X. Li, Y. J. Gu and W. T. Wong, *Int. J. Nanomed.*, 2020, **15**, 10271–10284.

28 C. Gellini and A. Feis, *Photoacoustics*, 2021, **23**, 100281.

29 M. W. Ji, M. Xu, W. Zhang, Z. Z. Yang, L. Huang, J. J. Liu, Y. Zhang, L. Gu, Y. X. Yu, W. C. Hao, P. F. An, L. R. Zheng, H. S. Zhu and J. T. Zhang, *Adv. Mater.*, 2016, **28**, 3094–3101.

30 X. Y. Xu, Y. Chong, X. Y. Liu, H. Fu, C. G. Yu, J. Huang and Z. J. Zhang, *Acta Biomater.*, 2019, **84**, 328–338.

31 J.-Z. Du, H.-J. Li and J. Wang, *Acc. Chem. Res.*, 2018, **51**, 2848–2856.

32 L. Y. Wang, J. Huang, H. B. Chen, H. Wu, Y. L. Xu, Y. Li, H. Yi, Y. A. Wang, L. Yang and H. Mao, *ACS Nano*, 2017, **11**, 4582–4592.

33 H. Yang, X. Heng and J. Hu, *RSC Adv.*, 2012, **2**, 12648–12651.

34 E. C. Cho, J. Xie, P. A. Wurm and Y. Xia, *Nano Lett.*, 2009, **9**, 1080–1084.

35 R. Wei, Z. Cai, B. W. Ren, A. Li, H. Lin, K. Zhang, H. Chen, H. Shan, H. Ai and J. Gao, *Chem. Mater.*, 2018, **30**, 7950–7961.

36 R. Wei, K. Liu, K. Zhang, Y. Fan, H. Lin and J. Gao, *ACS Appl. Mater. Interfaces*, 2022, **14**, 3784–3791.

37 S. Ruan, C. Hu, X. Tang, X. Cun, W. Xiao, K. Shi, Q. He and H. Gao, *ACS Nano*, 2016, **10**, 10086–10098.

38 P. Y. Huang, Y. Y. Zhu, H. Zhong, P. L. Chen, Q. Y. Shi, J. Y. Chen, J. M. Lai, Y. F. Tu, S. W. Liu and L. H. Liu, *Biomater. Sci.*, 2022, **10**, 1267–1280.

39 L. Wang, H. Lin, X. Chi, C. Sun, J. Huang, X. Tang, H. Chen, X. Luo, Z. Yin and J. Gao, *Small*, 2018, **14**, 1801612.

40 L.-S. Lin, Z.-X. Cong, J.-B. Cao, K.-M. Ke, Q.-L. Peng, J. Gao, H.-H. Yang, G. Liu and X. Chen, *ACS Nano*, 2014, **8**, 3876–3883.